



## Heterostructured TiO<sub>2</sub>/WO<sub>3</sub> Nanocomposites for Photocatalytic Degradation of Toluene under Visible Light

Li Zhang,<sup>a,b</sup> Mingke Qin,<sup>b</sup> Wei Yu,<sup>b,z</sup> Qinghong Zhang,<sup>a</sup> Hongyong Xie,<sup>b,z</sup> Zhiguo Sun,<sup>b</sup> Qian Shao,<sup>c</sup> Xingkui Guo,<sup>c</sup> Luhan Hao,<sup>d</sup> Yongjun Zheng,<sup>e</sup> and Zhanhu Guo<sup>d,\*</sup>

<sup>a</sup>State Key Laboratory for Modification of Chemical Fibers and Polymer Materials, College of Materials Science and Engineering, Donghua University, Shanghai 201620, People's Republic of China

<sup>b</sup>School of Environmental and Materials Engineering, Shanghai Second Polytechnic University, Shanghai 201209, People's Republic of China

<sup>c</sup>College of Chemical and Environmental Engineering, Shandong University of Science and Technology, Qingdao 266590, People's Republic of China

<sup>d</sup>Integrated Composites Lab (ICL), Department of Chemical & Biomolecular Engineering, University of Tennessee, Knoxville, Tennessee 37966, USA

<sup>e</sup>Department of Chemical and Environmental Engineering, Anyang Institute of Technology, Anyang, Henan 455000, People's Republic of China

Toluene, as a strong carcinogen, is widely found in the newly renovated rooms, shopping malls, and workshops. Photocatalytic oxidation has great superiority and application prospects for the degradation of toluene. However, low photocatalytic efficiency under visible-light irradiation arising from easy agglomeration of the solid catalysts hinders their photodegradation of toluene gas. In this work, heterostructured TiO<sub>2</sub>/WO<sub>3</sub> photocatalysts were fabricated via an electrospinning technology combining the hydrothermal treatment. The special microstructure and composition allowed the photogenerated electrons quickly transfer from the TiO<sub>2</sub> nanofibers to the WO<sub>3</sub> nanorods, and thus effectively reduced the recombination of photogenerated electrons and holes. Coupling TiO<sub>2</sub> with the narrow band-gap WO<sub>3</sub> broadened the spectral response range of TiO<sub>2</sub>. The heterostructured TiO<sub>2</sub>/WO<sub>3</sub> photocatalysts exhibited a remarkably higher degradation rate of toluene gas than that of the bare TiO<sub>2</sub> nanofibers under visible-light irradiation. The photocatalysts were deposited onto the inner walls of the photoreactor and some nylon meshes. The meshes were also placed in the photoreactor in a direction perpendicular to the air flow. The meshes increased the contact between photocatalysts in solid phase and toluene in gas phase, and about 85.3% of the toluene had been degraded in the experimental conditions. © 2017 The Electrochemical Society. [DOI: 10.1149/2.0881714jes] All rights reserved.

Manuscript submitted July 28, 2017; revised manuscript received November 7, 2017. Published December 6, 2017.

With the rapid development of industries, indoor air quality has attracted more and more attentions. The main reason for indoor air pollution is the release of large quantity of volatile organic compounds (VOCs) from the adhesives and paints used in the interior building materials.<sup>1</sup> Toluene is a common and typical VOC and has been recognized as a strong carcinogen. Both adsorption and photocatalytic degradation are considered as the most effective approaches to eliminate these pollutants.<sup>2</sup> Adsorption method could transfer VOCs from air to activated carbon, molecular sieve or other similar materials. However, the adsorbent has its maximum adsorption capacity, the desorption and regeneration processes may even cause secondary pollution.<sup>3</sup> Nowadays, photocatalytic oxidation technology is widely studied to degrade gaseous pollutants.<sup>4</sup> Under the ultraviolet or visible-light irradiation, the photocatalysts like TiO<sub>2</sub> generate electrons and holes, which are further converted to the hydroxyl radicals (OH•), superoxide anions (O<sub>2</sub>•<sup>-</sup>) and other active groups.<sup>5-8</sup> The VOCs can be oxidized by these active groups to form CO<sub>2</sub>, H<sub>2</sub>O and other inorganic small molecules.<sup>9</sup> But until now, the issues including low photocatalytic efficiency under visible-light irradiation and easy agglomeration of the solid catalysts hinder the deployment of this technique for removing toluene gas.<sup>10</sup>

Doping TiO<sub>2</sub> with other elements has been demonstrated to be an effective way to extend the spectral response from UV to visible region. For example, Asahi et al. found that the TiO<sub>2</sub> doped with N was visible-light active owing to the interaction between the N<sub>2p</sub> orbitals and the O<sub>2p</sub> orbitals, which led to the up-shifting of TiO<sub>2</sub> valence band.<sup>11</sup> Fuente et al. studied the doping of anatase TiO<sub>2</sub> with nine different dopants, and they found that W was one of the best options for toluene photodegradation using sunlight-type excitation.<sup>12</sup> In recent years, coupling TiO<sub>2</sub> with a narrow band-gap semiconductor to broaden the spectral response range and to retard photogenerated carrier recombination has attracted considerable attentions. Some semiconductor-semiconductor heterostructural nanomaterials, such as TiO<sub>2</sub>/CdS, TiO<sub>2</sub>/Bi<sub>4</sub>Ti<sub>3</sub>O<sub>12</sub>, and TiO<sub>2</sub>/WO<sub>3</sub>, have been studied.<sup>13-17</sup>

However, CdS is toxic and it is complex to be processed into ternary semiconductors such as Bi<sub>4</sub>Ti<sub>3</sub>O<sub>12</sub>. While WO<sub>3</sub> is harmless, it is worth to further study the TiO<sub>2</sub>/WO<sub>3</sub> heterostructures.

In the gas-solid heterogeneous photocatalytic degradation of VOCs, it is essential to select a suitable catalyst carrier. Unlike uniform dispersion of the catalyst in the liquid occurred in the photocatalytic degradation of wastewater, the solid phase photocatalysts in the photocatalytic degradation of VOCs are difficult to be uniformly dispersed in the gas pollutants. Thus, the catalysts need to be placed on a carrier such as molecular sieves, glass flakes, or inner walls of the photoreactor.<sup>18</sup> However, as the surface areas of these carriers are limited, the quantity of photocatalysts on the carriers is thus limited.

Herein, heterostructured TiO<sub>2</sub>/WO<sub>3</sub> nanocomposites were fabricated via a hydrothermal treatment of the electrospun TiO<sub>2</sub> nanofibers. The photocatalysts were deposited onto the inner walls of the photoreactor and some nylon meshes. The meshes were also placed in the photoreactor in a direction perpendicular to the air flow. Thus, the quantity of photocatalysts was increased, and the contact between photocatalysts and toluene was improved. Moreover, compared with the photocatalysts in the form of solid particles, the photocatalysts in the form of nanofibers had a fluffy internal structure and thus were more conducive to the passage of toluene gas. The photocatalytic activity of the heterostructured TiO<sub>2</sub>/WO<sub>3</sub> was investigated on the degradation of toluene gas under visible-light irradiation. The photocatalytic mechanism of the heterostructured TiO<sub>2</sub>/WO<sub>3</sub> was discussed in detail.

### Experimental

**Materials.**—Tetrabutyl titanate (Ti(OC<sub>4</sub>H<sub>9</sub>)<sub>4</sub>, 97%), acetic acid (glacial, 99.9%), tungstic acid (H<sub>2</sub>WO<sub>4</sub>), ethanol (C<sub>2</sub>H<sub>5</sub>OH, 99.9%), and toluene (C<sub>7</sub>H<sub>8</sub>, 99.5%) were all obtained from Sinopharm Chemical Reagent Co., Ltd. The TiO<sub>2</sub> nanoparticles (P25, 20% rutile and 80% anatase) were purchased from Evonik. Hydrogen peroxide (H<sub>2</sub>O<sub>2</sub>, 30%) and hexamethylenetetramine (HMT, C<sub>6</sub>H<sub>12</sub>N<sub>4</sub>, 99%) were purchased from Shanghai Titan Technology Co., Ltd. Poly(vinyl pyrrolidone) (PVP, M<sub>w</sub> ≈ 1.3 × 10<sup>6</sup>) was purchased from

\*Electrochemical Society Member.

<sup>z</sup>E-mail: yuwei@spsu.edu.cn; hyxie@spsu.edu.cn; zguo10@utk.edu

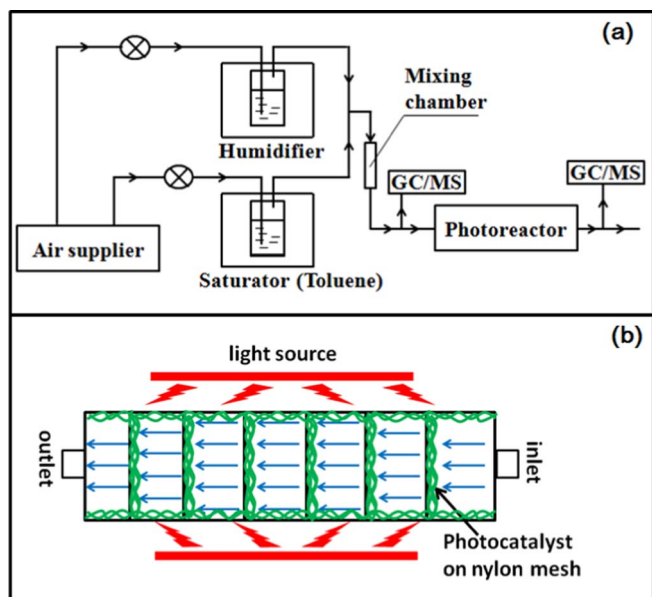


**Figure 1.** Schematic diagrams of the flow direction of the gas in the photodegradation experiment (a) and the placement of the nylon mesh deposited with photocatalyst in the photoreactor (b).

Sigma-Aldrich. All the chemicals were used as-received without any treatments.

**Synthesis of heterostructured  $\text{TiO}_2/\text{WO}_3$  nanocomposites.**—The bare  $\text{TiO}_2$  nanofibers were fabricated by electrospinning.<sup>19</sup> The growth of  $\text{WO}_3$  nanorods on the  $\text{TiO}_2$  nanofibers can be briefly described as follows. Typically, 24 mL 30 wt%  $\text{H}_2\text{O}_2$  was added into a beaker which contained 2.0 g  $\text{H}_2\text{WO}_4$  powders, and the beaker was heated at 95°C with continuous stirring. Then 56 mL  $\text{H}_2\text{O}$  was added into the solution, and a transparent sol was obtained. By dipping  $\text{TiO}_2$  nanofibers into the transparent sol for 30 min, a  $\text{WO}_3$  seed layer was deposited onto the  $\text{TiO}_2$  nanofibers, which were then collected and annealed at 300°C for 10 min. The treated  $\text{TiO}_2$  nanofibers were then added into a 50 mL stainless Teflon-lined autoclave containing 30 mL  $\text{H}_2\text{O}$ , 10 mL as-prepared transparent sol and 0.168 g  $\text{C}_6\text{H}_{12}\text{N}_4$  powders. Then the autoclave was sealed and maintained at 180°C for 10 h in an oven. The obtained products were collected and washed with ethanol and deionized water for additional three times and then dried in an oven at 60°C.

**Sample characterization.**—Field emission scanning electron microscopy (FESEM, Hitachi S-4800) and high-resolution transmission electron microscopy (HRTEM, JEOL JEM-2100 F) were used to characterize the morphologies of the products. For TEM measurement, the samples were dispersed ultrasonically in ethanol and then transferred onto carbon-coated copper grids. X-ray diffraction (XRD) was carried out on a Rigaku-D/max 2550 PC (Japan) diffractometer with  $\text{Cu K}_\alpha$  radiation ( $\lambda = 1.5406 \text{ \AA}$ ). UV-Vis diffuse reflectance (DRS) spectra were recorded on a PerkinElmer Lambda 950 instrument, using  $\text{BaSO}_4$  as the reference sample, in the range of 200–800 nm. Element contents were measured by an energy dispersive X-ray spectrometer (EDX-720, Shimadzu).

**Photoreactivity measurements.**—The photoreactor and experimental set-up used for the photodegradation of toluene were designed and built according to the reported procedures.<sup>20,21</sup> Briefly, the saturated toluene gas was prepared by passing air through a saturator containing liquid toluene (Figure 1a). The humidified air stream was generated by bubbling air through a thermostated glass bottle containing deionized water. Then the saturated toluene gas was mixed and diluted with humidified air stream at the gas mixer (mixing chamber).

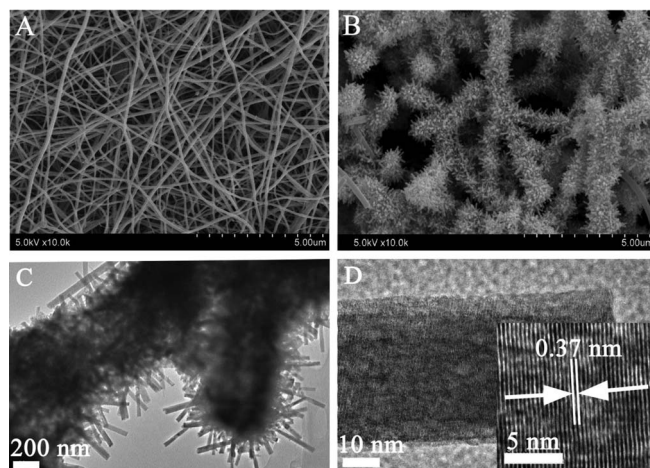


**Figure 2.** SEM images of the  $\text{TiO}_2$  nanofibers (a) and heterostructured  $\text{TiO}_2/\text{WO}_3$  nanocomposites (b); TEM images of the heterostructured  $\text{TiO}_2/\text{WO}_3$  nanocomposites (c) and  $\text{WO}_3$  nanorod (d). The inset in (d) is the HRTEM image of the  $\text{WO}_3$  nanorod.

The obtained toluene gas stream entered into the photoreactor with a constant flow rate of 400 standard cubic centimeter per min (sccm). The inlet toluene concentration was in the range between 300 and 400  $\text{mg/m}^3$  and the relative humidity was about 80%. The feed toluene concentration and relative humidity were set by varying the ratio of gas flow rates and/or varying the saturator temperature. The photoreactor was built with two fluorescent lamps (Philips TL-D 36W/54-765), and a quartz tube with an inner diameter of 80 mm and an effective length of 1200 mm. In this experiment, two fluorescent lamps were placed in the outside along the photoreactor to give 12  $\text{mW/cm}^2$  fluorescent irradiation with the spectrum in the visible region. The spectral range of the fluorescent lamp is 380–680 nm with three main emission peaks at 440, 555, and 590 nm, respectively. The  $\text{TiO}_2/\text{WO}_3$  nanocomposites were deposited onto some nylon meshes and the inner walls of the quartz tube, as shown in Figure 1b. The nylon meshes with the same size as the inner diameter of the photoreactor were also placed in the photoreactor in a direction perpendicular to the air flow. The average weight of photocatalysts in one piece of nylon mesh was  $\sim 0.025 \text{ g}$ . The air stream was sampled every 30 min at both the inlet and outlet using the Tenax tubes at a flow rate of 0.5 L/min for 1–5 min. The toluene in the tube was refilled every 3 hours to make sure a constant concentration of toluene. The toluene concentration of the air stream was analyzed by gas chromatography/mass spectrometry (GC/MS, Shimadzu QP2010 plus). The degradation degree DD (%) of toluene was calculated as follows:

$$DD = (C_i - C_o) \times 100 / C_i \quad [1]$$

where  $C_i$  is the inlet concentration and  $C_o$  is the outlet concentration at steady state.

## Results and Discussion

Figures 2a and 2b shows the typical SEM images of the  $\text{TiO}_2$  nanofibers and the heterostructured  $\text{TiO}_2/\text{WO}_3$  nanocomposites. The  $\text{TiO}_2$  nanofibers are continuous and form an unwoven mesh, with a diameter of  $\sim 250 \text{ nm}$ , as shown in Figure 2a. The heterostructured  $\text{TiO}_2/\text{WO}_3$  nanocomposites show a hierarchical structure, where the tiny  $\text{WO}_3$  nanorods are uniformly distributed across the entire surface of each  $\text{TiO}_2$  nanofiber forming a network of relief features (Figure 2b). The diameter of the  $\text{TiO}_2/\text{WO}_3$  nanocomposites is  $\sim 1000$  nanometers. TEM images confirm that the tiny  $\text{WO}_3$  nanorods grow vertically above the  $\text{TiO}_2$  nanofibers, and the length of the  $\text{WO}_3$  nanorods is  $\sim 200 \text{ nm}$  (Figure 2c). A close observation of the  $\text{WO}_3$  nanorod reveals that the  $\text{WO}_3$  nanorods are well crystallized with a diameter of  $\sim 40 \text{ nm}$  (Figure 2d). The lattice fringes on the nanorod

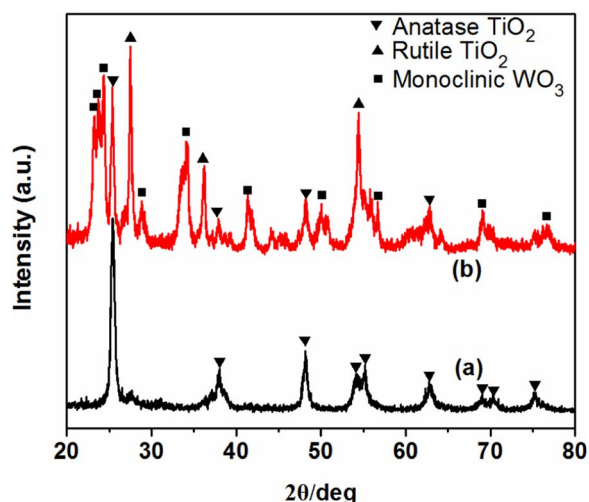


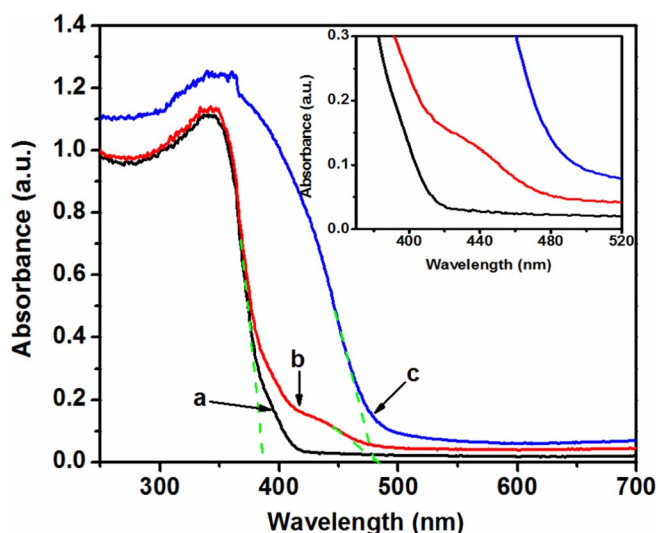
**Figure 3.** XRD patterns of the bare TiO<sub>2</sub> nanofibers (a) and the heterostructured TiO<sub>2</sub>/WO<sub>3</sub> nanocomposites (b).

indicate that WO<sub>3</sub> processes a single crystal structure. The inset in Figure 2d shows a high-resolution TEM (HRTEM) image recorded from the edge of one WO<sub>3</sub> nanorod. The fringe spacing of 0.37 nm corresponds to the spacing of the (0 0 2) lattice planes of WO<sub>3</sub>.<sup>22</sup> The content of WO<sub>3</sub> in the catalyst is calculated to be ~44.6% from the energy dispersive X-ray spectrometer (EDX) measurement.

X-ray diffraction (XRD) analysis is employed to investigate the crystal phases of the TiO<sub>2</sub> nanofibers and the heterostructured TiO<sub>2</sub>/WO<sub>3</sub> nanocomposites. Figure 3a shows the XRD patterns of the bare TiO<sub>2</sub> nanofibers, in which all the diffraction peaks are indexed as anatase TiO<sub>2</sub> (JCPDS 21-1272).<sup>23</sup> The XRD patterns of the TiO<sub>2</sub>/WO<sub>3</sub> nanocomposites show three crystal phases of anatase TiO<sub>2</sub>, rutile TiO<sub>2</sub>, and monoclinic WO<sub>3</sub> (Figure 3b). Treating the anatase TiO<sub>2</sub> nanofibers in an acidic solution, part of the anatase TiO<sub>2</sub> crystallites in the nanofibers were converted to the rutile TiO<sub>2</sub> crystallites in the nanofibers. The characteristic triple peaks at 23.15–24.35° and the diffraction peaks at 28.8°, 34.2° and 49.9° are indexed as monoclinic WO<sub>3</sub> (JCPDS 43-1035).<sup>24</sup> The crystallite sizes are 32.5, 38.9 and 21.4 nm for anatase TiO<sub>2</sub>, rutile TiO<sub>2</sub> and WO<sub>3</sub> after calcinations, respectively, calculated from X-ray line broadening ( $\omega$ ) according to the Scherrer formula:<sup>25</sup>

$$d = 0.89\lambda / \omega \cos \theta \quad [2]$$

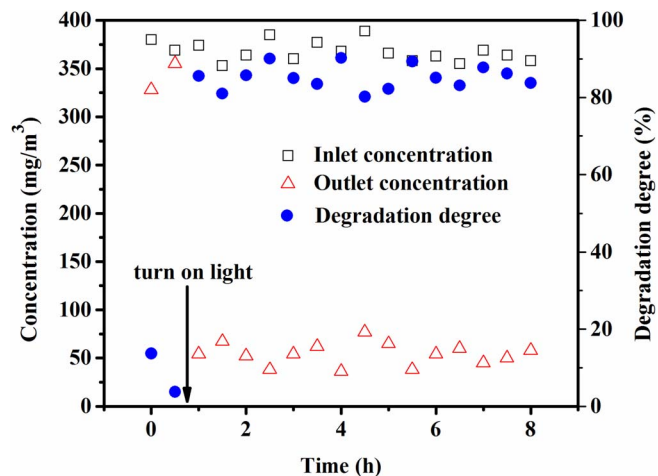
where  $\lambda$  is the X-ray wavelength, 1.5406 Å (Cu K $\alpha$ ), and  $\theta$  is the diffraction angle. Both oxides in the heterostructured TiO<sub>2</sub>/WO<sub>3</sub> nanocomposites exist as separated phases, and no indication of mixed compounds can be observed from the peaks in Figure 3b. A significant degree of preferred orientation could be deduced from the relative intensities of the characteristic triple peaks at 23.15–24.35°. The relative intensity of  $I_{002}/I_{020}/I_{200}$  for the heterostructured TiO<sub>2</sub>/WO<sub>3</sub> nanocomposites is 77/86/100, somewhat different from the reported 100/97/99 (JCPDS 43-1035). The increasing relative intensity of the (0 0 2) peak of the TiO<sub>2</sub>/WO<sub>3</sub> nanocomposites indicates the oriented growth of the nanorods in a preferential direction along *c* axis during the hydrothermal treatment. During hydrothermal treatment, the anatase TiO<sub>2</sub> crystallites in the nanofibers may change into the rutile TiO<sub>2</sub> crystallites which have a poor photocatalytic activity. However, the heterostructured TiO<sub>2</sub>/WO<sub>3</sub> photocatalysts could not be fabricated simultaneously just by electrospinning technology due to different spinning parameters of the TiO<sub>2</sub> and WO<sub>3</sub> precursor solutions. If TiO<sub>2</sub> and WO<sub>3</sub> nanofibers were individually spun and collected on the same collection device at the same time, the two fibers were only physically mixed, and the interface between them would not be high. Moreover, though rutile TiO<sub>2</sub> has a poor photocatalytic activity, it has been reported that the coexistence of anatase TiO<sub>2</sub> and rutile TiO<sub>2</sub> is conducive to improving the catalyst activity.<sup>26</sup>



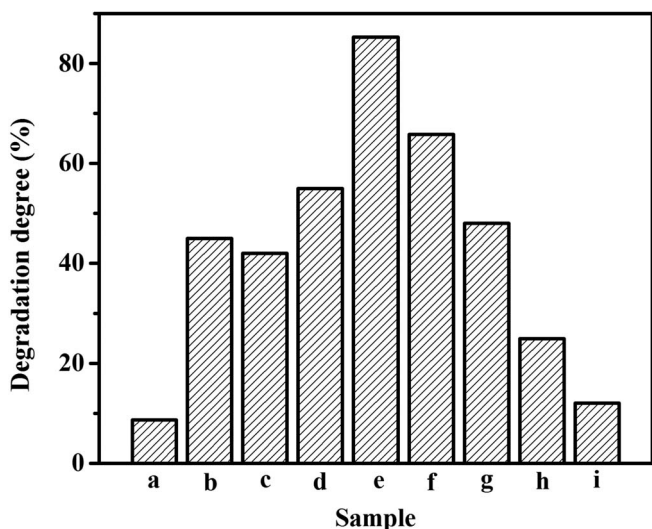
**Figure 4.** UV-vis diffuse reflectance spectra (DRS) of the bare TiO<sub>2</sub> nanofibers, the heterostructured TiO<sub>2</sub>/WO<sub>3</sub> nanocomposites, and WO<sub>3</sub> nanoparticles.

Figure 4 shows the UV-vis DRS of the bare TiO<sub>2</sub> nanofibers, the heterostructured TiO<sub>2</sub>/WO<sub>3</sub> nanocomposites, and WO<sub>3</sub> nanoparticles. It can be observed that the absorption edge for the heterostructured TiO<sub>2</sub>/WO<sub>3</sub> nanocomposite sample is shifted toward the visible region compared to that of the bare TiO<sub>2</sub> nanofibers. The main absorption edge for the bare TiO<sub>2</sub> nanofibers is estimated to be 389 nm, which can be attributed to the intrinsic absorption band derived from the bandgap transition (Figure 4a).<sup>27</sup> Compared with the bare TiO<sub>2</sub> nanofibers, the heterostructured TiO<sub>2</sub>/WO<sub>3</sub> nanocomposites present two absorption edges located at about 389 and 475 nm (Figure 4b), which are attributed to the intrinsic absorption band derived from the bandgap transition of TiO<sub>2</sub> and WO<sub>3</sub>, respectively. The WO<sub>3</sub> bandgap energy is calculated to be 2.6 eV using the relation  $E_g = 1240/\lambda$ ,<sup>28</sup> where  $\lambda$  is the onset absorption wavelength of 475 nm, as shown in Figure 4c. After coupling with the narrow band-gap WO<sub>3</sub>, the heterostructured TiO<sub>2</sub>/WO<sub>3</sub> nanocomposites increased the utilization of visible light, which could accordingly lead to a higher visible photocatalytic activity.

Figure 5 shows the typical measurement results of inlet and outlet concentrations versus time for toluene. The average initial



**Figure 5.** Typical measurement results of inlet and outlet concentrations versus time for toluene (samples of heterostructured TiO<sub>2</sub>/WO<sub>3</sub> nanocomposites; initial concentration of 300–400 mg/m<sup>3</sup>; relative humidity of 80%).



**Figure 6.** The average degradation degree over different samples: (a) heterostructured  $\text{TiO}_2/\text{WO}_3$  nanocomposites on six pieces of nylon mesh in dark; (b) P25, (c)  $\text{TiO}_2$  nanofibers, (d)  $\text{WO}_3$  nanoparticles, (e) heterostructured  $\text{TiO}_2/\text{WO}_3$  nanocomposites. The samples from (b) to (e) were all deposited on six pieces of nylon mesh under fluorescent light irradiation. The samples from (f) to (h) were all heterostructured  $\text{TiO}_2/\text{WO}_3$  nanocomposites, deposited on four pieces (f), two pieces (g) and zero pieces (h) of nylon mesh under fluorescent light irradiation. (i) no photocatalysts in the photoreactor under fluorescent light irradiation.

concentration was  $368 \text{ mg/m}^3$ , and the relative humidity was 80%. Six pieces of nylon mesh (400 mesh) deposited with the heterostructured  $\text{TiO}_2/\text{WO}_3$  nanocomposites were placed in the photoreactor perpendicular to the airflow. Before the fluorescent lights were turned on, the differences of the concentrations at the outlet and the inlet were not very obvious. However, after turning on the fluorescent lights, the concentrations at the outlet dropped drastically, while the concentrations at the inlet were relatively stable in the next four hours. The degradation degree could thus be obtained (Figure 5), and about 85.3% of the toluene was calculated to be degraded in the experimental conditions.

Figure 6 shows the average degradation degree over different samples. A blank test (without catalyst) under the fluorescent lamp irradiation exhibited little photodegradation. The average degradation degree with the sample of heterostructured  $\text{TiO}_2/\text{WO}_3$  nanocomposites on six pieces of nylon mesh in dark was similar to that of the blank test. The samples from (b) to (e) in Figure 6 are all deposited on six pieces of nylon mesh under fluorescent light irradiation. The heterostructured  $\text{TiO}_2/\text{WO}_3$  nanocomposites show a higher degradation degree than P25, the  $\text{TiO}_2$  nanofibers, and the  $\text{WO}_3$  nanoparticles. It benefits from the hierarchical structure which can hinder the recombination of the electrons and holes, and thus improve the photocatalytic efficiency. The samples from (f) to (h) in Figure 6 were all heterostructured  $\text{TiO}_2/\text{WO}_3$  nanocomposites, deposited on four pieces (f), two pieces (g) and zero pieces (h) of nylon mesh under fluorescent lamp irradiation. With increasing the number of nylon mesh in the photoreactor, the contact between the photocatalysts and the toluene gas also increased, thus the degradation degree was improved.

As shown in the schematic diagram of the hierarchical heterostructure (Figure 7), the  $\text{TiO}_2$  nanofibers and the  $\text{WO}_3$  nanorods are in close contact with each other, which can facilitate the photogenerated electrons or holes transfer from one semiconductor to another. The  $\text{WO}_3$  nanorods are single crystal structure, thus the transport of electrons will not be hindered by grain boundaries. This may facilitate the separation of the photogenerated carriers and improve the photocatalytic reaction rate.<sup>29–32</sup> The transfer of photogenerated carriers between  $\text{TiO}_2$  and  $\text{WO}_3$  is accompanied by the consecutive  $\text{W}^{6+}$  reduction into  $\text{W}^{5+}$  by capturing the photogenerated electrons at the trapping sites in  $\text{WO}_3$ .<sup>33</sup> Simultaneously, the  $\text{W}^{5+}$  on the surface of  $\text{WO}_3$  nanorods

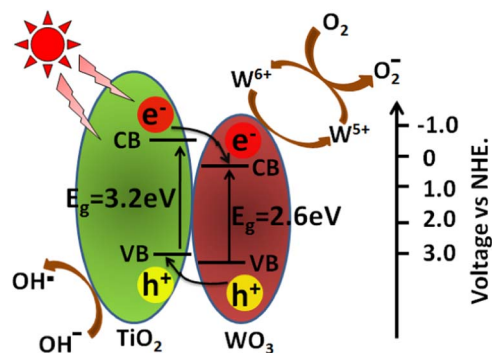


**Figure 7.** Schematic diagram showing the energy band structure and electron-hole pair separation in the heterostructured  $\text{TiO}_2/\text{WO}_3$  nanocomposites.

are reoxidized into  $\text{W}^{6+}$  by oxygen ( $\text{O}_2$ ), and  $\text{O}_2$  is subsequently reduced into  $\text{O}_2^{\bullet-}$ . The recycling of the electrons leads to an increase in the lifetime of the photogenerated electron-hole pairs and as a consequence to a promotion of the utilization of photons during the degradation of toluene. The holes are then captured by the hydroxyl groups ( $\text{OH}^-$ ) on the photocatalyst surface and generated hydroxyl radicals ( $\text{OH}^\bullet$ ).<sup>34–36</sup> The formed superoxide anions ( $\text{O}_2^{\bullet-}$ ) may either attack toluene directly or generate the hydroxyl radicals ( $\text{OH}^\bullet$ ) by reacting with the photogenerated electrons and the hydrogen ions ( $\text{H}^+$ ).<sup>37,38</sup> Finally, the strong oxidizing agents hydroxyl radicals ( $\text{OH}^\bullet$ ) degrade toluene into small molecules.

## Conclusions

Heterostructured  $\text{TiO}_2/\text{WO}_3$  photocatalysts were fabricated via an electrospinning technology combining the hydrothermal treatment. The hierarchical heterostructure demonstrated enhanced visible-light absorption and increased photocatalytic degradation of toluene. Under visible-light irradiation, the migration of electron-hole pairs between  $\text{TiO}_2$  and  $\text{WO}_3$  increased the lifetime of the charge carriers, which was beneficial for improving the photoactivity. Increasing the number of nylon mesh from zero to six increased the content of photocatalysts in the photoreactor, the degradation degree was also increased. This study provides a new route to solve the issue of insufficient contact between the contaminants and the photocatalyst in the gas-solid reactions.

## Acknowledgments

The project was funded by State Key Laboratory for Modification of Chemical Fibers and Polymer Materials, Donghua University (No. LK1518), Natural Science Foundation of Shanghai (Nos. 16ZR1412600, 15ZR1416900), Natural Science Foundation of China (Nos. 51476094, 51590901), Shanghai Eastern Professorship grant, Shu Guang project supported by Shanghai Municipal Education Commission and Shanghai Education Development Foundation (No. 15SG52).

## References

1. M. Hussain, N. Russo, and G. Saracco, *Chem. Eng. J.*, **166**, 138 (2011).
2. Y. F. Cao, J. G. Wang, J. Q. Qiao, H. X. Wan, H. X. Li, and J. Zhu, *Acta Chim. Sinica*, **71**, 567 (2013).
3. W. W. Yuan, P. Yuan, D. Liu, L. L. Deng, J. M. Zhou, W. B. Yu, and F. R. Chen, *Chem. Eng. J.*, **294**, 333 (2016).
4. H. Kunkely and A. Vogler, *Inorg. Chem. Commun.*, **24**, 134 (2012).
5. Y. J. Jiang and R. Amal, *Appl. Catal. B: Environ.*, **138–139**, 260 (2013).
6. X. M. Xiang, F. P. Pan, and Y. Li, *Adv. Compos. Hybrid Mater.*, in press, (2017).
7. B. Song, T. T. Wang, H. G. Sun, Q. Shao, J. K. Zhao, K. K. Song, L. H. Hao, L. Wang, and Z. Guo, *Dalton Trans.*, in press, (2017).
8. L. Zhang, Y. G. Li, Q. H. Zhang, G. Y. Shi, and H. Z. Wang, *Chem. Lett.*, **40**, 1371 (2011).
9. R. Jothiramingam and M. K. Wang, *J. Hazard. Mater.*, **147**, 562 (2007).
10. Z. Liu, P. F. Fang, S. J. Wang, Y. P. Gao, F. T. Chen, F. Zheng, Y. Liu, and Y. Q. Dai, *J. Mol. Catal. A-Chem.*, **363–364**, 159 (2012).
11. R. Asahi, T. Morikawa, T. Ohwaki, K. Aoki, and Y. Taga, *Science*, **293**, 269 (2001).

12. A. Fuerte, M. D. Hernández-Alonso, A. J. Maira, A. Martínez-Arias, M. Fernández-García, J. C. Conesa, and J. Soria, *Chem. Commun.*, **24**, 2718 (2001).
13. K. Zhao, Z. M. Wu, R. Tang, Y. D. Jiang, and Y. X. Lu, *Res. Chem. Intermediat.*, **41**, 4405 (2015).
14. T. P. Cao, Y. J. Li, C. H. Wang, Z. Y. Zhang, M. Y. Zhang, C. L. Shao, and Y. C. Liu, *J. Mater. Chem.*, **21**, 6922 (2011).
15. A. Cordero-García, G. T. Palomino, L. Hinojosa-Reyes, J. L. Guzman-Mar, L. Maya-Tevinno, and A. Hernandez-Ramirez, *Environ. Sci. Pollut. R.*, **24**, 4613 (2017).
16. S. J. Li, S. W. Hu, W. Jiang, Y. Liu, J. S. Liu, and Z. H. Wang, *J. Colloid Interf. Sci.*, **501**, 156 (2017).
17. Y. N. Feng, X. D. Jiang, E. Ghafari, B. Kucukgok, C. Y. Zhang, I. Ferguson, and N. Lu, *Adv. Compos. Hybrid Mater.*, in press, (2017).
18. S. Adjimi, N. Sergent, J. C. Roux, F. Delpéch, M. Pera-Titus, K. Chhor, A. Kanaev, and P. X. Thivel, *Appl. Catal. B: Environ.*, **154–155**, 123 (2014).
19. L. Zhang, Y. G. Li, Q. H. Zhang, and H. Z. Wang, *CrystEngComm*, **15**, 5986 (2013).
20. H. Y. Xie, Y. N. Zhang, and Q. L. Xu, *J. Nanosci. Nanotechnol.*, **10**, 5445 (2010).
21. L. Zhang, Y. G. Li, H. Y. Xie, H. Z. Wang, and Q. H. Zhang, *J. Nanosci. Nanotechnol.*, **15**, 2944 (2015).
22. X. L. Li, T. J. Lou, X. M. Sun, and Y. D. Li, *Inorg. Chem.*, **43**, 5442 (2004).
23. L. Zhang, Q. H. Zhang, H. Y. Xie, J. Guo, H. L. Lyu, Y. G. Li, Z. G. Sun, H. Z. Wang, and Z. Guo, *Appl. Catal. B: Environ.*, **201**, 470 (2017).
24. B. Yang, Y. J. Zhang, E. Drabarek, P. R. F. Barnes, and V. Luca, *Chem. Mater.*, **19**, 5664 (2007).
25. P. Mavinakuli, S. Y. Wei, Q. Wang, A. B. Karki, S. Dhage, Z. Wang, D. P. Young, and Z. Guo, *J. Phys. Chem. C*, **114**, 3874 (2010).
26. H. Tong, S. X. Ouyang, Y. P. Bi, N. Umezawa, M. Oshikiri, and J. H. Ye, *Adv. Mater.*, **24**, 229 (2012).
27. A. W. Morawski, E. Kusiak-Nejman, J. Przepiorski, R. Kordala, and J. Pernak, *Celulose*, **20**, 1293 (2013).
28. C. F. Lin, C. H. Wu, and Z. N. Onn, *J. Hazard. Mater.*, **154**, 1033 (2008).
29. Y. Z. Zhu, Z. X. Xu, Q. Q. Lang, W. Y. Jiang, Q. Q. Yin, S. X. Zhong, and S. Bai, *Appl. Catal. B: Environ.*, **206**, 282 (2017).
30. Z. Sun, L. Zhang, F. Dang, Y. Liu, Z. Fei, Q. Shao, H. Lin, J. Guo, L. Xiang, N. Yerra, and Z. Guo, *CrystEngComm*, **19**, 3288 (2017).
31. Y. Li, X. Wu, J. Song, J. Li, Q. Shao, N. Cao, N. Lu, and Z. Guo, *Polymer*, **124**, 41 (2017).
32. C. Cheng, R. Fan, Z. Wang, Q. Shao, X. Guo, P. Xie, Y. Yin, Y. Zhang, L. An, Y. Lei, J. Ryu, A. Shankar, and Z. Guo, *Carbon*, **125**, 103 (2017).
33. V. Keller, P. Bernhardt, and F. Garin, *J. Catal.*, **215**, 129 (2003).
34. H. W. Huang, Y. He, R. He, X. X. Jiang, Z. S. Lin, Y. H. Zhang, and S. C. Wang, *Inorg. Chem. Commun.*, **40**, 215 (2014).
35. K. Zhang, G. Li, L. Feng, N. Wang, J. Guo, K. Sun, K. Yu, J. Zeng, T. Li, Z. Guo, and M. Wang, *J. Mater. Chem. C*, **5**, 9359 (2017).
36. T. Liu, K. Yu, L. Gao, H. Chen, N. Wang, L. Hao, T. Li, H. He, and Z. Guo, *J. Mater. Chem. A*, **5**, 17848 (2017).
37. O. Legrini, E. Oliveros, and A. M. Braun, *Chem. Rev.*, **93**, 671 (1993).
38. L. Zhang, W. Yu, C. Han, J. Guo, Q. H. Zhang, H. Y. Xie, Q. Shao, Z. G. Sun, and Z. Guo, *J. Electrochem. Soc.*, **164**, H651 (2017).